

pubs.acs.org/acsaelm Article

# Controlled Phase Stabilization Enabled Tunable Optical Properties of Nanocrystalline GeO<sub>2</sub> Films

Paul Gaurav Nalam, Debabrata Das, Susheng Tan, and Chintalapalle V. Ramana\*



Cite This: ACS Appl. Electron. Mater. 2022, 4, 3115-3124



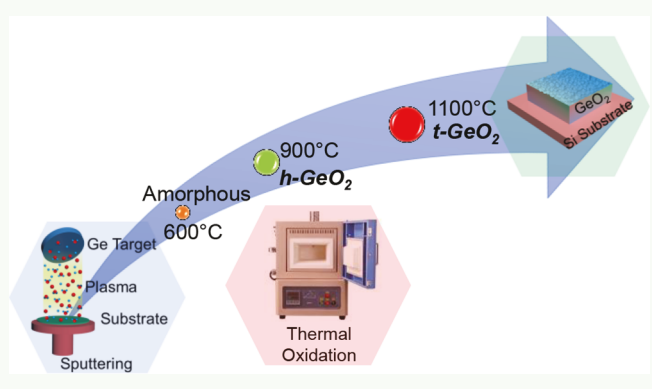
**ACCESS** I

Metrics & More

Article Recommendations

s Supporting Information

**ABSTRACT:** Germanium oxide  $(GeO_2)$  exhibits two polymorphs, namely,  $\alpha$ -quartz and rutile, which belongs to the ultrawide band gap (UWBG) semiconductor group. With exceptional thermal conductivity and ambipolar capability by doping,  $GeO_2$  has tremendous prospects for next-generation semiconductor electronics and other multifunctional device applications. However, the primary bottleneck for  $GeO_2$  utilization in advanced applications is the complexity in selectively synthesizing the desired polymorph with a controlled phase and properties. Free formation energies of these polymorphs are relatively close to each other and prone to stabilize in various metastable states or a complex mixture of respective phases. In this context, we present an approach to successfully demonstrate nanotextured hexagonal



(h) and tetragonal (t) phases of  $GeO_2$  on Si and quartz substrates through a hybrid synthesis route, which involves film deposition by magnetron sputtering followed by postdeposition thermal oxidation. The resulting  $GeO_2$  thin films exhibit exceptional optical behavior with a high band gap at 6.21 eV for the  $\alpha$ -quartz phase and 5.29 eV for the rutile phase. Precise control over the deposition and annealing conditions under oxygen atmosphere results in the formation of amorphous (a) and crystalline phases of  $GeO_2$  films. The evolution of h-GeO<sub>2</sub> and t-GeO<sub>2</sub> phases is further analyzed using a variety of analytical methods selectively determining the crystal structure, surface morphology, and optical properties. The findings of the current study can be further endorsed while fabricating phase-pure bulk and nanostructured  $GeO_2$  on numerous platforms as a potential candidate for UWBG semiconductors for advanced technological applications.

KEYWORDS: GeO2, nanocrystalline thin film, hexagonal GeO2, tetragonal GeO2, optical properties

### INTRODUCTION

By virtue of excellent properties coupled with exceptional thermal and chemical stability, ultrawide band gap (UWBG) semiconductors are receiving significant attention by the research community for their utilization in a multitude of scientific and technological applications. These UWBG semiconductors hold promise to meet the emerging needs and demands of the current and future technologies. Germanium dioxide (GeO<sub>2</sub>), which is one among the UWBG oxide semiconductors, has steadily gained attention recently in the landscape of high-power electronics, deep-UV optoelectronics/ photonics, and energy storage applications because of its versatile properties. Because of the prodigious thermal, electronic, and optical properties of the different phases, GeO<sub>2</sub> is considered to hold immense application potential in semiconductor electronics, energy storage, and optical waveguide technologies. 11–13

GeO<sub>2</sub> exists primarily in two phases, that is,  $\alpha$ -quartz (hexagonal structure) and rutile (tetragonal) phases. <sup>14–16</sup> Both the polymorphs of GeO<sub>2</sub> fall into the class of UWBG semiconductors with a band gap significantly higher than 4

eV, while conventional semiconductors are in the range of 0.5–4.0 eV. <sup>17</sup> With higher carrier mobility and better ambipolar dopability, GeO<sub>2</sub> can be a perfect material of choice for homoepitaxially grown *p-n* junction-based next-generation efficient electronic and optoelectronic devices. <sup>18,19</sup> GeO<sub>2</sub> is theoretically anticipated to have a higher intrinsic phonon-limited thermal conductivity (37 W m<sup>-1</sup> K<sup>-1</sup> along the *a* direction and 58 W m<sup>-1</sup> K<sup>-1</sup> along the *c* direction at 300 K) than others which belong to the same class of UWBG semiconductors. <sup>17</sup> Previous reports have theoretically predicted a high p and n Baliga Figure of Merit for the GeO<sub>2</sub> rutile phase, which can be beneficial while designing power devices with higher block-in voltage with improved on-set carrier conductivity. <sup>18,20</sup> Despite the ideal properties for various

Received: April 27, 2022 Accepted: May 18, 2022 Published: June 8, 2022





applications, GeO2 suffers from the lack in ability to conveniently synthesize nanostructured thin films with a controlled microstructure and crystal phase. This scientific challenge stems from the fact that GeO2 exhibits polymorphism. Because the free energy of formation of these polymorphs is relatively close, it increases the possibility of forming deep metastable states. 19,21 This makes attaining and fine-tuning of the synthesis conditions for a specific crystal phase with controlled morphology and texturing at the nanoscale dimensions challenging. The glassy phase of GeO<sub>2</sub> is the easiest to form at close to room-temperature conditions. The h-GeO<sub>2</sub> unit cell has a volume  $\approx$ 40% less than the t-GeO<sub>2</sub> phase which creates more complications in processing the material with a stabilized phase.<sup>22\*</sup>Furthermore, because of the aforementioned reasons, complex or elevated processing conditions, such as high-pressure (>100 MPa) conditions during synthesis or phase conversion, are desired to obtain specific GeO<sub>2</sub> polymorphs. <sup>22,23</sup> Thus, phase stabilization with a controlled structure and properties of GeO2 is a continuing problem for both experimental and theoretical studies.

To address the fundamental scientific challenge of phase stabilization, in this work, we have adopted a hybrid approach, which is based on sputtering of Ge under partial  $Ar/O_2$  pressure followed by thermal oxidation at elevated temperature. With preoptimized sputtering of  $Ge-GeO_2$  nanocomposite thin films, followed by precisely controlled thermal oxidation, we have successfully demonstrated tailoring of nanotextured  $GeO_2$  between h- and t- phases. A schematic of the hybrid synthesis process employed in this work to realize phase-controlled  $GeO_2$  is schematically presented in Figure 1,

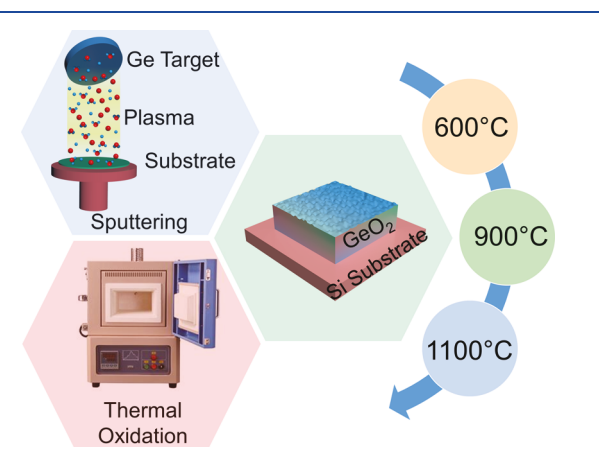


**Figure 1.** Schematic of the hybrid synthesis process (sputter deposition followed by thermal oxidation) to stabilize nanocrystalline  $h\text{-GeO}_2$  and  $t\text{-GeO}_2$  phases on Si and quartz.

where the evolution of the as-deposited a-phase Ge-GeO $_2$  thin film into temperature-induced nanocrystalline h-GeO $_2$  and t-GeO $_2$  phase formation is evident. Detailed structural, topographical, and optical investigations illuminate the evolution of GeO $_2$  from h- to t-phase with corresponding modulation of its primitive material characteristics. These findings can provide a roadmap to further tune the conditions so as to design phase-selective multifunctional GeO $_2$  films or nanostructures for advanced scientific or technological applications.

### MATERIALS AND METHODS

**Synthesis of Nanostructured GeO<sub>2</sub> Thin Films.** We adopted a hybrid synthesis route to fabricate nanostructured GeO<sub>2</sub> films with in

situ phase controllability. Initial deposition was performed under precisely controlled  ${\rm Ar/O_2}$  plasma followed by postdeposition processing under a controlled thermo-chemical atmosphere. The purpose of the postdeposition processing is simply the thermal oxidation and crystallization at different temperatures.

GeO<sub>2</sub> films were deposited onto silicon (100) and quartz substrates using radio-frequency magnetron sputtering. Excel instruments radiofrequency magnetron sputter model-DCSS12 is used to deposit the thin films. A schematic diagram of the deposition system employed to fabricate GeO<sub>2</sub> films is presented in Figure S1. The substrates used were thoroughly cleaned with acetone, methanol, and deionized water sequentially, before introducing them into the sputter chamber. A 2" 99.999% pure Ge target (Plasmaterial Inc.) was used for deposition. The sputter-deposition chamber was pumped down to a base pressure of 1.5  $\times$  10<sup>-7</sup> Torr before deposition using a roughing pump and a turbo pump. High-purity (99.999%) Ar and O2 gases were used in the sputtering chamber for the deposition. The flow rate of gases was controlled using MKS multigas controllers. The preoptimized ratio of Ar/O2 (20 sccm/20 sccm) mixed with plasma was used to ablate the Ge target and to deposit the Ge-GeO2 complex composite on the Si substrate. The power of the plasma source was controlled at 100 W. The pressure during deposition was optimized at  $1 \times 10^{-2}$  Torr, and the substrate temperature was kept at 600 °C to provide an amorphous SiO<sub>2</sub> interface for initial nucleation. Also, the deposition time was kept constant (2 h) to obtain a uniform thickness of the samples. The subsequent steps involved postdeposition processing in a furnace to allow for thermal-oxidation and thermally induced crystallization. Under this step, the samples were heat-treated at temperatures ranging from 800 to 1100 °C for 2 h. The samples were set to the desired temperature by means of a heating rate of 10 °C/ min, and the samples were cooled down, after the completion of the process, at a cooling rate of 5 °C/min.

**Characterization.** X-ray Diffraction (XRD). XRD measurements on the GeO<sub>2</sub> thin films were conducted using a Malvern Panalytical Empyrean Nano edition multipurpose X-ray diffractometer. The X-ray diffractometer was used in Bragg—Brentano reflection geometry. To resolve each peak from the diffraction pattern clearly,  $\theta/2\theta$  scans with a step size of 0.01° and an integration time of 0.6 s/step were conducted on the thin films at room temperature. A Cu K $\alpha$  X-ray source with a wavelength of 0.154 nm was used to acquire the measurements. Strong peaks from the silicon substrate were observed but are not included in the figures for convenience. Rietveld refinement in Xpert highscore software was used to understand precise changes in lattice parameters with respect to standard powder diffraction data. The Scherrer relationship was used to calculate the crystalline size and strain from the peak broadening in the XRD scans. The Scherrer equation is defined by: <sup>24</sup>

$$D_{hkl} = \frac{K\lambda}{\beta \cos\theta} \tag{1}$$

where  $D_{hkl}$  is the crystallite size,  $\lambda$  is the wavelength of the, K is the shape factor with a value close to unity  $\approx$ 0.9,  $\beta$  is the full width half maximum, and  $\theta$  is the Bragg angle or angle of the peak.

Transmission Electron Microscopy (TEM). The TEM characterization of GeO2 films was carried out on a Thermo Scientific (formerly FEI) Titan Themis 200 G2 probe aberration-corrected system equipped with a SuperX energy-dispersive X-ray spectrometer (EDS). The TEM was operated at 200 kV. Our previously established procedures for wide band-gap oxides, especially for sample preparation as well as detailed characterization, were employed in this work for GeO<sub>2</sub> films. <sup>25,26</sup> For TEM analyses, the GeO<sub>2</sub> specimens were prepared using a FEI Scios focused ion beam (FIB) and a scanning electron microscope (SEM) dual beam system following a standard protocol for TEM specimen preparation. First, using an electron beam at 5 kV 1.6 nA a thin carbon protection layer of 15  $\mu$ m  $\times$  2  $\mu$ m was deposited on the Ga<sub>2</sub>O<sub>3</sub> film grown on a Si substrate, and then using a Ga ion beam a 15  $\mu$ m  $\times$  2  $\mu$ m  $\times$  2  $\mu$ m Pt protection film was deposited on top of the carbon protection layer at 30 kV 300 pA followed by rough cutting, cleaning cut, J-cut, and lamellae transfer

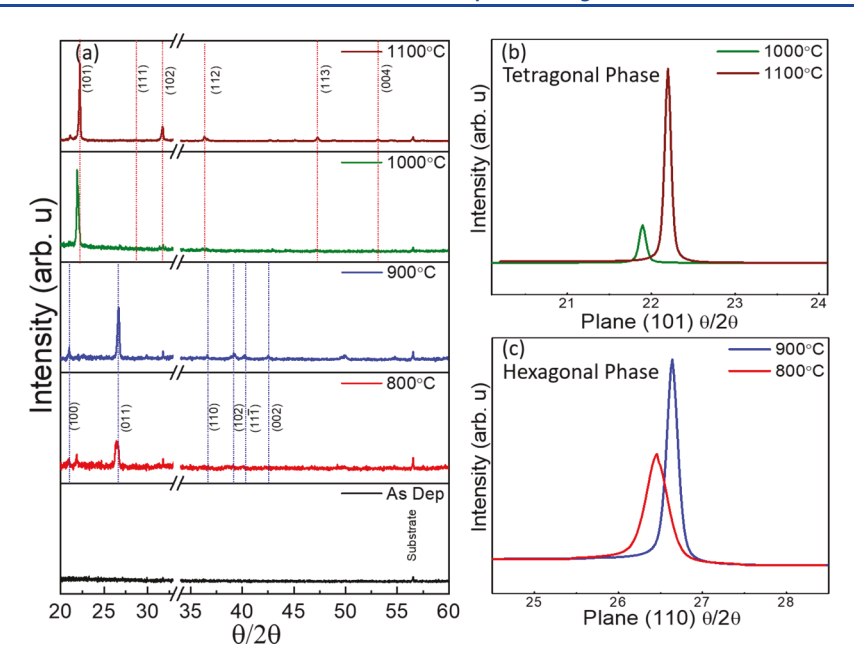


**Figure 2.** (a) XRD spectra of the as deposited a-phase and the postdeposition thermally oxidized h-GeO<sub>2</sub> and t-GeO<sub>2</sub> thin films on silicon. (b) Peak from the (101) plane of t-phase GeO<sub>2</sub> after thermal oxidation at 1000 and 1100 °C. (c) Peak from the (110) plane of t-phase GeO<sub>2</sub> after thermal oxidation at 800 and 900 °C.

out of the substrate to a TEM grid.<sup>25</sup> The final thinned specimen of about 80 nm was further FIB cleaned at 5 kV 48 pA and 2 kV 27 pA, respectively, to remove excess amorphotized and contaminated layers. TEM data processing, if any, was carried out using the relevant offline data processing software from Thermo Scientific. Fiji ImageJ was also employed to run radial profile analysis using selective area electron diffraction (SAED).<sup>25</sup>

Chemical analysis and homogeneity analysis of the  ${\rm GeO_2}$  films were performed using high-angle annular dark-field scanning transmission electron microscopy (HAADF-STEM), which is quite useful in evaluating the nanocrystalline materials. Elemental mapping was carried out with a SuperX X-ray energy-dispersive spectrometer (EDS) on a Thermo Scientific Titan Themis G2 200 Probe Cs-corrected transmission electron microscope in scanning transmission mode (STEM) with an HAADF detector. The camera length was 110 mm and the collection angle was 46–220 mrad. Elemental maps were acquired with a nanoprobe of 20 pixels and a beam current of 100 pA at 512  $\times$  512 pixels and 20 us dwell time.

Atomic Force Microscopy (AFM). The surface topography measurements were performed using the Nanosurf Naio AFM. The conical AFM tips used were from Nanoscience Instruments with a spring constant of 0.1 N/m and a radius of curvature of 8 nm. Other important parameters of the AFM tip include a resonant frequency of 28 kHz, length of 225  $\mu$ m, a width of 42  $\mu$ m, and a thickness of 0.9  $\mu$ m. The AFM tips have a 30 nm aluminum reflex coating on the detector side of the cantilever for better reflectance of the laser beam, as this AFM works using the beam bounce method of detection. All the scans are performed in contact mode with a set point of 10 nN, which was optimized to reveal clear surface morphologies of crystal growth in the thin film. The scans were acquired under a constant feedback method to control the perpendicular motion of the tip from the thin film surface. Multiple scans for each thin film contributed to a conclusive roughness analysis. 5  $\times$  5  $\mu$ m and 1  $\times$  1  $\mu$ m scans are acquired with 300 points/line and a time per line of 4 s. The proportionality gain and integral gain were set at 10000 and 1000, respectively. WSXM and Gwyddion software were used to analyze the roughness properties and to remove surface artifacts in the AFM scans. The 2D AFM scan were parabolically flattened and smoothened using the Gaussian fit to level and remove noise in the

Spectroscopic Ellipsometry (SE). SE was performed on the asdeposited and heat-treated films using the Semilab SE-2000 spectroscopic ellipsometer. The scans were performed in multiple regions of the film to validate the data received. The wavelength range over which the optical parameters were obtained is 200–2000 nm with a step size of 1 nm, three angles of incidence (65,70, and 75°) were chosen around the principle angle of reflectance to validate and receive accurate chi and delta values. Sam Suite V1.3.1.4 and Spectroscopic Ellipsometry Analyzer v1.6.6.2 software were used for spectroscopic ellipsometry data acquisition and modeling, respectively.

Optical Spectroscopy (UV–vis–NIR). Optical properties of  $GeO_2$  films were measured in the wavelength range of 200-2500 nm. Spectral characteristics of the films were measured in the broad ultraviolet(UV), visible, and near infrared (NIR) regions. This range of the electromagnetic spectrum falls well within the excitation zones of the possible crystal structures in the  $GeO_2$  system. A Jasco V-770 UV–vis spectrophotometer, equipped with an integrating sphere, was used for data acquisition.

Direct transmission spectroscopy was adopted for accurate measurement of band edge absorption. Similar samples were prepared on quartz substrates and characterized with XRD measurement, prior to the optical spectroscopy, to confirm stabilization of equivalent phases similar to the samples on Si/SiO<sub>2</sub> substrates. The importance of this step in characterization is to state a clear understanding of GeO<sub>2</sub> thin films in a more revealing transmission mode instead of the standard reflectance mode (for Si/SiO<sub>2</sub> substrates). Therefore, because both quartz and silicon substrates are amorphous on the surface of the substrates it is understood that there is no substrate-related texturing of the thin film. This analysis was done with quartz substrates only to understand the effect of phase transformation on electronic transitions and band gap of GeO<sub>2</sub> films.

## ■ RESULTS AND DISCUSSION

**Crystal Structure and Phase.** *X-ray Diffraction.* The XRD patterns obtained from the  $GeO_2$  thin films as-deposited and postdeposition thermal annealing at different temperatures are shown in Figure 2a. The diffraction patterns  $(\theta/2\theta \text{ scans}, \text{range } 20-60^\circ)$  reveal clear crystallization of two different phases of  $GeO_2$  in the thin films thermally oxidized at higher temperatures. While the diffraction pattern from the asdeposited  $GeO_2$  thin film at 600 °C shows amorphous

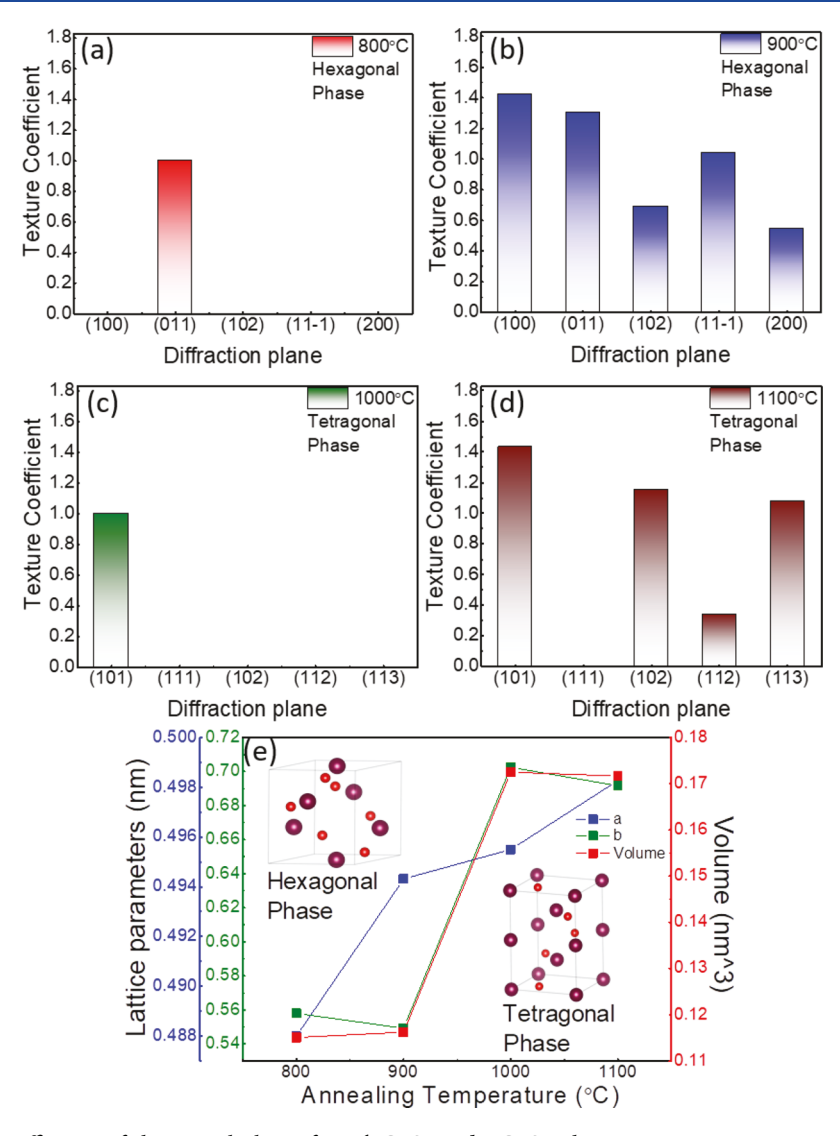


Figure 3. (a-d) Texture coefficients of the critical planes from h-GeO<sub>2</sub> and t-GeO<sub>2</sub> phases at various temperatures of thermal oxidation. (e) Variation of lattice parameters and volume of h-GeO<sub>2</sub> and t-GeO<sub>2</sub> phases with respect to thermal oxidation temperature.

characteristics, the thermally oxidized films (800–1100  $^{\circ}$ C) revealed the presence of two distinct phases, namely, hexagonal (with space group P 32 2 1 (#154)) and the tetragonal (space group P41212 (#92)). The characteristic peaks are quantified for each sample to determine the crystal structure and the phase stabilization. Figure 2b,c shows the comparison of absolute intensity and full width at half maximum (FWHM) between the most dominated peaks in h- and t-GeO $_2$  phases. A summary of the crystallographic data, such as the diffraction planes and their corresponding intensities along with the standard intensities, is shown in the Supporting Information (Tables S1 and S2).

The crystal structures of the films were refined on Xpert high score using Rietveld refinement, and the goodness of fit is below 5 for the acquired lattice parameters. We adopted the refinement procedures and parameters, as described in ref 25. applicable for intrinsic and doped wide band gap oxides. The values of the refined lattice structures in GeO<sub>2</sub> are shown in the Supporting Information (Table S3).

The XRD patterns obtained for annealed films ( $T_{\rm ann} \geq 800$  °C) reveal the diffraction peaks indicating the crystallization of GeO<sub>2</sub>. At 800 °C, the diffraction pattern shows properties of

partial crystallization in the h-phase, although the overall crystallinity of the sample is still amorphous. The peak profile for the most preferred plane (011) at 26.5° has a higher relative FWHM and confirms higher density of defects and dislocations. This partial crystallization is attributed to the higher thermal energy required for atomic diffusion to enable complete crystallization of GeO2. Though there is no evidence of elemental Ge-related XRD peaks, optical transmission data show evidence of absorption in the NIR region (discussed in a later section). These lower energy transitions confirm the existence of interstitial states related to Ge. For the film heattreated at 900 °C, the diffraction pattern reveals the presence of other peaks from the h-phase, with higher intensity and lower broadening of the plane (011) indicating higher crystallinity. The texture analysis corroborates this observation. The texture coefficients were calculated using the formula: 25,28

$$T_{c} = \frac{I_{m}(hkl)/I_{o}(hkl)}{\frac{1}{n}\sum_{1}^{n}I_{m}(hkl)/I_{o}(hkl)}$$
(2)

 $T_{\rm c}$  is the texture coefficient,  $I_{\rm m}$  is the reflected intensity from the hkl crystallographic plane,  $I_{\rm o}$  is the standard intensity of the (hkl) plane form powder diffraction file, and n is the total

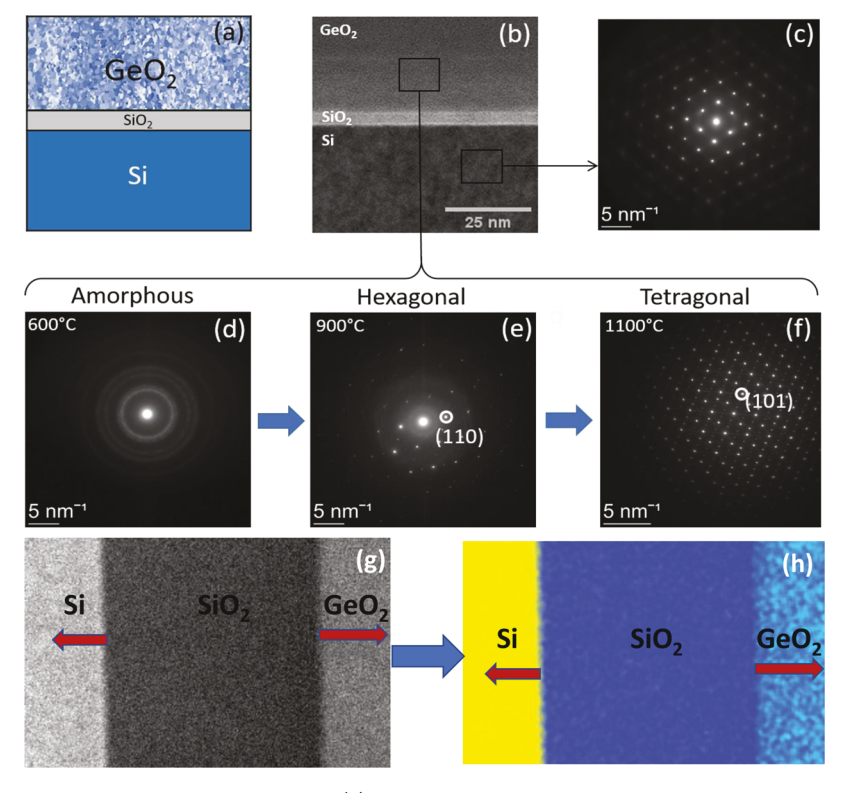


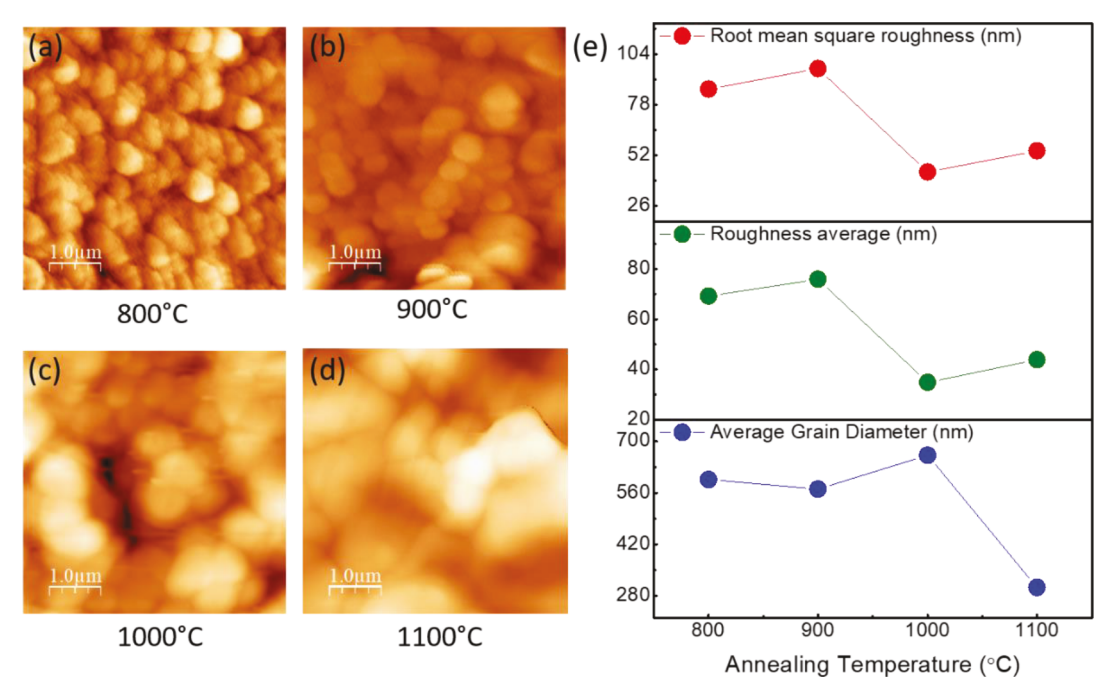
Figure 4. TEM data of GeO<sub>2</sub> films deposited on Si substrates. (a) Schematic of the nanotextured GeO<sub>2</sub> thin film on the Si substrate. (b) Cross-sectional TEM image of the GeO<sub>2</sub>/SiO<sub>2</sub>/Si interface. The regions of the GeO<sub>2</sub> film, SiO<sub>2</sub> interfacial layer, and Si substrate are as marked in the image. (c) SAED pattern of the silicon substrate. (d) SAED of as-deposited GeO<sub>2</sub> films. The nature of the electron diffraction pattern confirms the amorphous nature of the GeO<sub>2</sub> films. (e) SAED of GeO<sub>2</sub> films annealed at 900 °C. Formation of the *h*-phase GeO<sub>2</sub> films is evident. (f) SAED of GeO<sub>2</sub> films annealed at 1100 °C. Further structural transformation of GeO<sub>2</sub> films and stabilized *t*-phase is evident. (g, h) HAADF STEM image (g) and EDS map (h) of the GeO<sub>2</sub> films. These images indicate both the Si/SiO<sub>2</sub> interface and SiO<sub>2</sub>/GeO<sub>2</sub> interface regions, which confirm the structural integrity of the GeO<sub>2</sub> films deposited. The two chemically well-defined Si/SiO<sub>2</sub> and SiO<sub>2</sub>/GeO<sub>2</sub> interfaces are evident in these data.

number of reflections measured. The variation of  $T_c$  with temperature for various crystal planes is shown in Figure 3a-d.

On refinement of the films heat treated at 900 °C, the lattice structure is observed to shift significantly along the a direction from 0.488 to 0.494 nm, suggesting an increase in lattice volume moving closer to the standard lattice structure of h-GeO<sub>2</sub>. The films  $T_{\rm ann} \geq 1000$  °C do not have any characteristic peaks from the h-GeO<sub>2</sub> structure but fit well with the peaks present in the t-phase of GeO<sub>2</sub>. This unequivocally states that the films completely transform from h- to t-phase of GeO<sub>2</sub>. The strong texturing in (100) plane for h- lattice and (101) plane for t- lattice at the initial temperatures of crystallization is due to the lower surface free energy of these planes, however at higher temperatures other minor planes are revealed. Figure 3b,c indicates the most dominant peaks among both the phases.

Similar to the  $GeO_2$  films processed at 800 °C (h-phase), the  $GeO_2$  films at 1000 °C shows low crystallinity of the t-phase. In both cases, the texture coefficient (Figure 3) of corresponding crystal orientations ((011) in the h-phase and (101) in t-phase is relatively low along with a broader FWHM of respective peaks. The absence of remnant peaks of the previous hexagonal phase confirms recrystallization of  $GeO_2$  from h- to a t-structure. The (101) of the t-phase at this temperature is the most prominent diffraction peak with a slight shift to the left, indicating a higher lattice constant with a d-spacing of 0.405 nm relative to a d-spacing of 0.399 nm (Figure 3e) of the more stable and crystalline phase obtained at higher temperatures of heat treatment. This increase in the interplanar spacing of the

(101) plane in the GeO<sub>2</sub> films annealed at 1000 °C indicates its effect via lattice refinement with a significantly higher lattice constant in the c-direction and hence a higher volume of the crystal lattice (see, Figure 3e). This meta-stable state at 1000 °C of increased lattice volume of the *t*-phase is owed to higher lattice strain and dislocation density in the film, which is clear from the higher peak broadening (FWHM) in the diffraction pattern. The diffraction patterns from the GeO<sub>2</sub> films annealed at 1100 °C form a more stable t-phase, as they exhibit higher crystallinity with lower lattice strain and higher crystallite size. The peaks appear due to (112), (113), and (004) planes for GeO<sub>2</sub> films at 1100 °C which fit well to the t-lattice system of GeO<sub>2</sub>. It is important to note that the phase transformation from h- to t- also changes the coordination number of the Ge cation from 4 to 3 and Oxygen anion from 2 to 3, this moves the Ge ions from the t- sites into the (90, 90, and  $180^{\circ}$ ) trigonal planar sites. This change of atomic positions in the lattice structure results in the shift of the electron cloud overlap and therefore, the electron energy degeneracies in the crystal field. Thus, the detailed structural characterization reveals the evolution of different polymorphs, starting from a complex a- $GeO_2$  phase and then pure h- and t- phase stabilization with increasing thermal oxidation temperature. Comprehensive refinement of XRD peaks along with texture coefficient conveys the presence of multidirectional crystal orientation of corresponding phases depending on suitable formation energy provided during the postdeposition thermal oxidation synthesis process.



pubs.acs.org/acsaelm

Figure 5. (a–d) AFM scans indicating surface morphology of  $GeO_2$  thin films at different thermal oxidation temperatures (800, 900, 1000, and 1100 °C) respectively. (e) Variation of RMS, roughness average, and average grain diameter of nanocrystalline  $GeO_2$  thin films with respect to thermal oxidation temperatures.

Transmission Electron Microscopy. The TEM data (Figure 4) of GeO<sub>2</sub> films also provided a clear difference between the phases formed. The kinematic amplitudes of the electron diffraction from key reflecting planes in the phases present define the atomic positions of Ge and O atoms and provide insight into the progress of crystallinity with an increase in annealing temperature. Because TEM acquires data from higher energy electrons relative to the X-rays from XRD, the scans obtained are of significantly higher resolution and can resolve planes with much lower interplanar spacing.

Cross-sectional TEM images shown in Figure 4 indicate the stabilization of respective phases of GeO<sub>2</sub> films. Figure 4a shows the layout of the sample for all the deposition conditions employed. The bright interface between the thin film and Si substrate confirmed the existence of an interfacial SiO<sub>2</sub> layer (Figure 4b). The HAADF STEM cross section images, which are also shown in Figure 4, indicate the SiO<sub>2</sub> and Si substrate interfacial regions of GeO<sub>2</sub> film. The electron diffraction pattern from Si (Figure 4c) confirms the structural/crystal quality of the substrate. Two-step fabrication (sputtering and thermal oxidation) of the GeO<sub>2</sub> thin film on Si causes oxygen diffusion into the substrate forming the SiO2 interfacial layer. The electron diffraction patterns reconfirm the amorphous nature of the as-deposited GeO<sub>2</sub> films. The electron diffraction patterns of annealed GeO2 films clearly indicate crystalline nature (Figure 4e,f). The experimental electron diffraction patterns have the combined effect of the Lorentz-type geometric contributions, Debye-Waller radial dampening, and dynamic behavior of reflections.<sup>29</sup> Similar to the XRD observations, in TEM, we observe that the electron diffraction spots from the primary reflections in the 900 °C sample are farther from the central transmission beam in reciprocal space compared to the t-phase of the 1100 °C sample, where the radial distance corresponds to the inverse of interplanar spacing.

The primary reflections at two different annealing temperatures are indexed in Figure 4e,f. Because of the absence of rings and presence of clearly resolved diffraction spots, the thin films look well textured. Postdeposition thermal annealing induces crystallization and formation/stabilization of h- and t-phases of  ${\rm GeO}_2$  films annealed at respective temperatures. Perhaps, thermal energy provided under atmospheric pressure facilitates the crystallization and respective phase formation of  ${\rm GeO}_2$  thin films.

The HAADF-STEM images (Figure 4) indicate the chemically homogeneous and abrupt interfaces for  ${\rm GeO_2}$  films on Si substrates. The composition imaging analyses (Figure 4g,h) carried out by elemental mapping indicate that the  ${\rm GeO_2}$  is stoichiometric with a chemical composition well maintained for both as-deposited and heat-treated samples. Also, the images reveal that the chemical composition was uniform with chemically well-defined interfaces across Si,  ${\rm SiO_2}$ , and  ${\rm GeO_2}$  film regions.

**Surface Morphology.** The AFM scans (Figure 5) provided us with critical insights into the surface morphology of the GeO<sub>2</sub> films, especially as a function of phase transformations noted. The surface morphology of the asdeposited GeO2 films was characterized to be relatively flat with no distinct grain presence; this is typical behavior of amorphous surfaces.<sup>30</sup> However, as the temperature of thermal oxidation increases the AFM images start to reveal grain growth and crystallization with circular to oval morphologies. The average grain size, roughness average, and root mean square (RMS) average for all the scans were analyzed to quantify surface morphology of the thin films. The root mean square roughness  $(R_a)$  and the roughness average  $(\overline{h})$  (Figure 5) describe the height variation on the surface. These two characteristics related to surface morphology are calculated using<sup>25,31</sup>

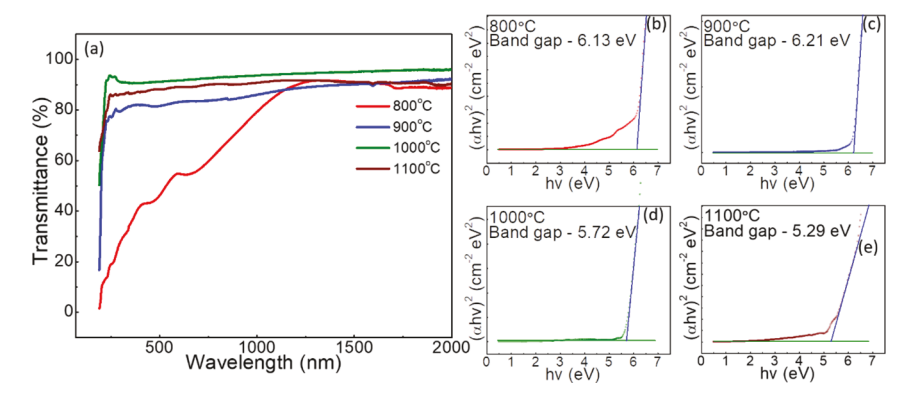


Figure 6. (a) Transmittance plots from the GeO<sub>2</sub>/quartz thin films. (b-e) Tauc plots form transmission data thermally oxidized at different temperatures. The intersects of the linear portion in the plots indicate the band gaps of the respective thin films.

$$R_{q} = \sqrt{\frac{1}{NM} \sum_{i=1}^{N} \sum_{j=1}^{M} [h(x_{i}, y_{j}) - \overline{h}]^{2}}$$
(3)

$$\overline{h} = \frac{1}{NM} \sum_{i=1}^{N} \sum_{j=1}^{M} h(x_i, y_j)$$
(4)

where  $h(x_i, y_j)$  is the surface height at a given point (x, y) and N and M are the number of points in the x and y directions.

The root mean square roughness values of the films tend to show a lower value for films at grain growth initiation and at phase transition. As the annealing temperature increases, for hand t- phases of GeO2, the roughness values increase with the increase in the crystallinity of the phase. This behavior of increase in h and Rq with the increase in heat treatment before phase transition and after phase transition further substantiates the effect of distinct crystal growth kinetics followed by the two phases formed in the GeO<sub>2</sub> thin films upon thermal treatment. The RMS roughness values for the h-GeO<sub>2</sub> films (86–97 nm) are observed to be generally higher than those for the t-GeO<sub>2</sub> films (43-64 nm). This switch of the surface morphology toward reduced roughness and larger indistinct grains after phase transition is attributed to the lower amount of intergrain free energy. This is due to the considerable difference in the texturing of the h- phase from the t- phase. The high texturing of the t- phase along the [101] direction relative to the hphase with significantly dissimilar planes of orientation perpendicular to the substrate causes lowering of the intergrain free energy after phase transition.

The grain diameter analysis was performed using ImageJ, and the values were averaged to calculate the average grain size of the films. The average grain diameter shows an increasing trend with an increase in crystallinity and encounters an intermediate morphological condition at 1000  $^{\circ}$ C where it adopts a more amorphous grain morphology as indicated in the XRD scans before completely crystallizing into the  $t\text{-GeO}_2$  phase grains.

Optical Properties. Optical Absorption and Band Gap. Because we established the crystallographic significance of heat-treated GeO<sub>2</sub> thin films, we now discuss the optical characteristics and correlate the physical properties with the optical properties of the films. The optical transmittance and Tauc plots of GeO<sub>2</sub> films are shown in Figure 6. The resultant band gap values determined for the *a*-GeO<sub>2</sub> films are similar to earlier studies on GeO<sub>2</sub>.<sup>33</sup> The GeO<sub>2</sub> thin films in the visible spectrum at the as-deposited condition look reddish brown

and are partly translucent, whereas on heat treatment of the samples ( $800-1100\,^{\circ}\text{C}$ ) they turn whitish yellow and opaque, similar to the observations made by Nunley et al. <sup>12</sup> An integration sphere is used to conduct diffused reflectance measurements in a UV–vis spectrophotometer. <sup>34</sup> The asdeposited film and the thermally oxidized film at 800 °C are observed to have a transmittance of about 87% in the range of 1690-2240 and 1260-2270 nm, respectively, but show a consistent decline in transmittance at higher energies. This lower degree of transmittance at lower temperatures of heat treatment is due to scattering of light by defects present in the films. We believe that these defects may be due to the presence of metallic Ge along with GeO<sub>2</sub>.

As the temperature increases, the defect density decreases because the Ge fully reacts with the oxygen and forms single-phase  ${\rm GeO_2}$ . The transmittance for the heat-treated films  $\geq 900$  °C show a high degree of transmittance throughout the spectrum in the range of 74–95% up to the energy at 200 nm. This high transmittance explains a much lower amount of optical scattering within the films. The film heat-treated at higher temperatures shows strong free exciton peaks at 243 nm (5.1 eV), particularly at 1000 °C where the exciton peak is pronounced. This observation of exciton in a thin film is usually a strong indication of the high quality of the phase formed in the film.

The optical absorption coefficient ( $\alpha$ ) was calculated from the optical transmittance and the thickness of the films using <sup>56,59</sup>:

$$\alpha(\lambda) = -\ln(T/t) \tag{5}$$

where T is transmittance,  $\lambda$  is wavelength, and t is the thickness of the films. The absorption coefficient  $(\alpha)$  relates to photon energy (h) for direct band gap using the following relation:

$$(\alpha h \nu)^2 = \beta (h \nu - E_{\rm g}) \tag{6}$$

where  $\beta$  is a constant called the band tailing parameter,  $E_{\rm g}$  is the energy of the optical band gap and the power of  $(\alpha h\nu)$  is determined by the transition mode.<sup>35</sup> The optical band gap was determined by plotting  $(\alpha h\nu)^2$  against the incident photon energy  $(h\nu)$  for the various films as shown in Figure 6 (Tauc plots). The values were determined upon extrapolating the linear portion of the Tauc plot.<sup>36,37</sup>

The bandgap determined for the as-deposited amorphous GeO<sub>2</sub> films is 5.21 eV, which is in good agreement with the value reported in the literature. Upon thermal annealing, the band gap value jumps to 6.09 eV. The band gap

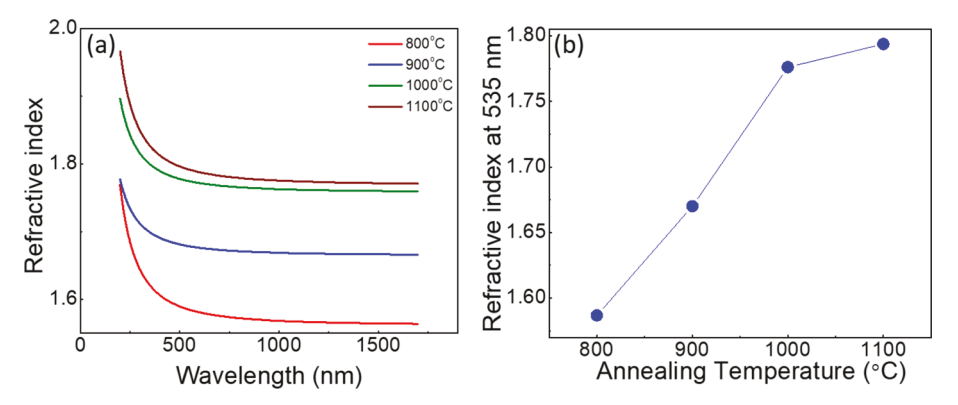


Figure 7. (a) Variation of the refractive index in GeO<sub>2</sub> thin films with respect to the temperature of thermal oxidation over a range of wavelengths (200–1700 nm). (b) Variation of the refractive index at 535 nm in GeO<sub>2</sub> thin films thermally oxidized at different temperatures.

corroborated with structural studies, which indicates that the crystallization of the GeO2 occurs with h-phase formation at 800 °C, the band gap increase to 6.09 eV is in accordance with phase transformation in the GeO2 films as a function of heat treatment. For GeO<sub>2</sub> films thermally annealed at 900 °C, the band gap determined from spectral data was 6.2 eV. However, it is quite interesting to note that the band gap relative to the film at 800 °C falls to 5.7 eV for 1000 °C for GeO2 films once the t-phase emerges. The bandgap stabilizes at 5.23 eV for GeO<sub>2</sub> films thermally annealed at 1100 °C. This trend in the behavior of GeO<sub>2</sub> films is highly correlated with the phase and the degree of disorder. The fundamental absorption edge also known as the Urbach tail below the exponential increase in the band gap energy can also quantify the degree of structural disorder in the films. The reasons for the presence of the Urbach tail in materials have been extensively investigated, which could be due to photon-phonon interactions, excitons, impurities, and structural disorders.<sup>38</sup> The Urbach tails in the films heat-treated ≤800 °C are more significant, correlating with their higher amount of optical scattering and structural disorder among other reasons. These Urbach tails for the heattreated films for temperatures ≥900 °C are not as pronounced.

Optical Constants (Refractive Index). The optical constants (Figure 7) of the films were determined using the spectroscopic ellipsometer at three different angles. The ellipsometer measures the relative changes in amplitude and phase of linearly polarized monochromatic light around the principle angle of reflectance from the film surface (chosen angles of incidence- 65, 70, 75°). The measured values from ellipsometry are the  $\Psi$  (azimuth) and  $\Delta$  (phase change), which give an insight into the optical properties and microstructure of the films. <sup>33,39</sup> The relation between these values is as follows:

$$\rho = \frac{R_{\rm p}}{R_{\rm s}} = \tan \Psi \exp(i\Delta) \tag{7}$$

where  $R_{\rm p}$  and  $R_{\rm s}$  are the complex reflection coefficients for light polarized parallel and perpendicular to the films plane of incidence. The above complex reflectance equation is used to derive the film thickness and refractive index by employing appropriate dispersion laws to model the acquired  $\Psi$  and  $\Delta$  values.

Ellipsometric analysis depends on the relation  $2n \ge z$ , where n is the number of observations and z are the parameters that need to be determined. This relation is used to validate the parameters determined from the complex reflectance ratios. Therefore, the observations are multiplied using various angles

of incidence over a wide spectrum of measurements. The measured values were best modeled using the single oscillator Sellmeier dispersion relation. <sup>40</sup> The formula is as follows.

$$n^2(\lambda) = 1 + B \frac{\lambda^2}{\lambda^2 - {\lambda_0}^2} \tag{8}$$

where n is the refractive index,  $\lambda$  is the wavelength of the incident light, B is a dimensionless parameter that defines the profile of refractive index curvature in the visible spectrum, and  $\lambda_0$  is the resonant wavelength. Here, it is important to understand that the Sellmeier dispersion relation is not consistent with Kramers–Kroning relation. Hence, the Sellmeier parameters cannot have a physical meaning. All other derivations need to be extracted from the refractive index.

Using the above relations, the n values are in a reasonable range of 1.45-1.8 at 525-2000 nm, relative to the crystallinity of individual GeO<sub>2</sub> films (Figure 7). The behavior of refractive index of the a-phase and the lower crystalline films at ≤800 °C heat treatment show similar values of 1.6 which are in agreement with the work published by other researchers.<sup>33</sup> As the temperature of thermal oxidation increases to 900  $^{\circ}$ C, the *n* value for the crystalline h-phase GeO<sub>2</sub> film increases to 1.67, whereas the *n* value for the 1000 °C heat-treated film increases to  $\approx 1.8$ . This is a clear indication of the change in optical properties with the increase in thermal oxidation temperature. From the n values measured, a close correlation between the crystalline phase formed and the refractive index is observed in the GeO<sub>2</sub> films (Figure 8). The refractive index of GeO<sub>2</sub> is well established (1.57), and our results are in agreement with those observed in the literature. 10,41

Considering aforementioned analyses, it is clear that the proposed hybrid synthesis route successfully produced phasecontrolled nanocrystalline GeO2 films on Si with excellent optical quality. Precise tailoring of h- and t-phases along with nanotextured morphology elevates the importance of this simple approach to synthesize GeO2 thin films for various scientific and technological applications. Detailed structural analysis revealed phase purity of the nanocrystalline films, whereas optical investigation showed its potential in deep UV region. To shed light on the usefulness of this work, we present a phase diagram in Figure 8, where the modulation of the optical band gap and refractive index (at 525 nm) of different phases can be noted. Starting with a-phase Ge-GeO<sub>2</sub> at 600 °C, a gradual evolution into h- and t- phases depending on postdeposition thermal oxidation conditions shows a clear evolution and performance of GeO<sub>2</sub> thin films at different

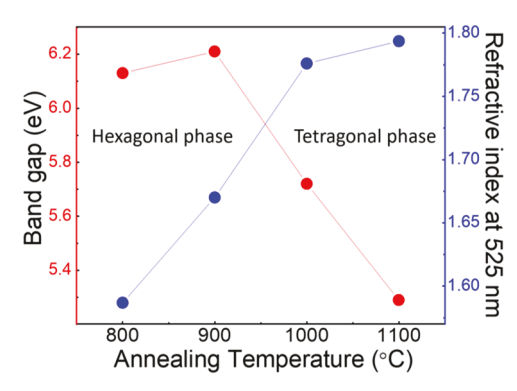


**Figure 8.** Relation between the band gap and refractive index of  $\text{GeO}_2$  thin films with respect to the variation of temperature during thermal oxidation.

temperatures. The most significant characteristic of the current approach is preoptimized deposition of the  ${\rm Ge-GeO_2}$  complex composite and controlled oxidation-assisted in situ tailoring of different  ${\rm GeO_2}$  phases leading to desirable optical property manipulation.

## SUMMARY AND CONCLUSIONS

Summarizing the results, we have demonstrated nanocrystalline  $GeO_2$  thin films in pure  $\alpha$ -quartz and rutile phases. Precisely controlled synthesis parameters demonstrated pure polymorphs of GeO2 on Si substrate. Structural and topographical characterization revealed gradual modulation of GeO<sub>2</sub> thin films from amorphous to phase pure tetragonal and hexagonal forms with nanotextured surface morphology. Cross-sectional TEM imaging and HAADF-STEM imaging analyses indicate the chemically homogenous and chemically well-defined abrupt GeO<sub>2</sub>/Si interface. SAED, collected from various nanospots of the thin film, was in good agreement with the structural characteristics and confirmed temperaturedependent stabilization of h- and t- phases. Detailed optical characterization portrayed band bag tailoring along with an improved refractive index in the UV-vis region which is common for such UWBG semiconductors. This hybrid synthesis method with precisely controlled process parameters has great potential to demonstrate phase-pure nanocrystalline GeO2 thin films with nanotextured surface morphology and reduced defect density. The current findings can be adopted further to fabricate GeO2 as an alternative UWBG metal oxide semiconductor for advanced scientific or technological innovations.

## ASSOCIATED CONTENT

#### Supporting Information

The Supporting Information is available free of charge at https://pubs.acs.org/doi/10.1021/acsaelm.2c00549.

Additional details of XRD calculations, the indexed peaks from the h-phase and t-phases, refined crystal structure data, comparison with the standard intensities of the respective h-phase and t-phase  $GeO_2$ , the schematic diagram, instrument details of the sputter-deposition system employed for  $GeO_2$  film fabrication, and the optical model fitting parameters for as-deposited and thermally annealed  $GeO_2$  films (PDF)

#### AUTHOR INFORMATION

## **Corresponding Author**

Chintalapalle V. Ramana — Centre for Advanced Materials Research (CMR) and Department of Mechanical Engineering, University of Texas at El Paso, El Paso, Texas 79968, United States; orcid.org/0000-0002-5286-3065; Email: rychintalapalle@utep.edu

#### Authors

Paul Gaurav Nalam – Centre for Advanced Materials Research (CMR) and Department of Mechanical Engineering, University of Texas at El Paso, El Paso, Texas 79968, United States

Debabrata Das — Centre for Advanced Materials Research (CMR) and Department of Mechanical Engineering, University of Texas at El Paso, El Paso, Texas 79968, United States; Occid.org/0000-0003-4326-6805

Susheng Tan — Department of Electrical and Computer Engineering and Petersen Institute of NanoScience and Engineering, University of Pittsburg, Pittsburgh, Pennsylvania 15261, United States; orcid.org/0000-0002-6162-7443

Complete contact information is available at: https://pubs.acs.org/10.1021/acsaelm.2c00549

#### **Notes**

The authors declare no competing financial interest.

#### ACKNOWLEDGMENTS

The authors acknowledge, with pleasure, support from the National Science Foundation (NSF) with NSF-PREM grant #DMR-1827745.

## **■** REFERENCES

- (1) Higashiwaki, M.; Kaplar, R.; Pernot, J.; Zhao, H. Ultrawide Bandgap Semiconductors. *Appl. Phys. Lett.* **2021**, *118*, 200401.
- (2) Jishi, R. A.; Appleton, R. J.; Guzman, D. M. Electronic and Optical Properties of Ultrawide Bandgap Perovskite Semiconductors via First Principles Calculations. *Appl. Phys. Lett.* **2020**, *117*, 232102.
- (3) Lu, Y.; Warner, J. H. Synthesis and Applications of Wide Bandgap 2D Layered Semiconductors Reaching the Green and Blue Wavelengths. ACS Appl. Electron. Mater. 2020, 2, 1777–1814.
- (4) Mubeen, S.; Hernandez-Sosa, G.; Moses, D.; Lee, J.; Moskovits, M. Plasmonic Photosensitization of a Wide Band Gap Semiconductor: Converting Plasmons to Charge Carriers. *Nano Lett.* **2011**, *11*, 5548–5552.
- (5) Fischetti, M. V.; Neumayer, D. A.; Cartier, E. A. Effective Electron Mobility in Si Inversion Layers in Metal—Oxide—Semi-conductor Systems with a High- $\kappa$  Insulator: The Role of Remote Phonon Scattering. *J. Appl. Phys.* **2001**, *90*, 4587–4608.
- (6) Klimm, D. Electronic Materials with a Wide Band Gap: Recent Developments. *IUCrJ* **2014**, *1*, 281–290.
- (7) Hebda, M.; Stochel, G.; Szaciłowski, K.; Macyk, W. Optoelectronic Switches Based on Wide Band Gap Semiconductors. *J. Phys. Chem. B* **2006**, *110*, 15275–15283.
- (8) Bush, K. A.; Frohna, K.; Prasanna, R.; Beal, R. E.; Leijtens, T.; Swifter, S. A.; McGehee, M. D. Compositional Engineering for Efficient Wide Band Gap Perovskites with Improved Stability to Photoinduced Phase Segregation. ACS Energy Lett. 2018, 3, 428–435.
- (9) Wang, S.; Ma, F.; Jiang, H.; Shao, Y.; Wu, Y.; Hao, X. Band Gap-Tunable Porous Borocarbonitride Nanosheets for High Energy-Density Supercapacitors. *ACS Appl. Mater. Interfaces* **2018**, *10*, 19588–19597.
- (10) Devyatykh, G. G.; Dianov, E. M.; Karpychev, N. S.; Mazavin, S. M.; Mashinskiĭ, V. M.; Neustruev, V. B.; Nikolaĭchik, A. V.; Prokhorov, A. M.; Ritus, A. I.; Sokolov, N. I.; Yushin, A. S. Material

- Dispersion and Rayleigh Scattering in Glassy Germanium Dioxide, a Substance with Promising Applications in Low-Loss Optical Fiber Waveguides. Sov. J. Quantum Electron. 1980, 10, 900.
- (11) Deng, G.; Saito, K.; Tanaka, T.; Arita, M.; Guo, Q. Pulsed Laser Deposition Growth of Ultra-Wide Bandgap GeO<sub>2</sub> Film and Its Optical Properties. *Appl. Phys. Lett.* **2021**, *119*, 182101.
- (12) Nunley, T. N.; Fernando, N. S.; Samarasingha, N.; Moya, J. M.; Nelson, C. M.; Medina, A. A.; Zollner, S. Optical Constants of Germanium and Thermally Grown Germanium Dioxide from 0.5 to 6.6 eV via a Multisample Ellipsometry Investigation. *J. Vac. Sci. Technol., B* **2016**, 34, No. 061205.
- (13) Ramana, C. V.; Carbajal-Franco, G.; Vemuri, R. S.; Troitskaia, I. B.; Gromilov, S. A.; Atuchin, V. V. Optical Properties and Thermal Stability of Germanium Oxide (GeO<sub>2</sub>) Nanocrystals with  $\alpha$ -Quartz Structure. *Mater. Sci. Eng., B* **2010**, *174*, 279–284.
- (14) Rathore, M. S.; Vinod, A.; Angalakurthi, R.; Pathak, A. P.; Thatikonda, S. K.; Nelamarri, S. R. Role of Oxygen Pressure on the Structural and Photoluminescence Properties of Pulsed Laser Deposited GeO<sub>2</sub> Thin Films. *Phys. B* **2022**, *625*, No. 413466.
- (15) Ramana, C. V.; Troitskaia, I. B.; Gromilov, S. A.; Atuchin, V. V. Electrical Properties of Germanium Oxide with  $\alpha$ -Quartz Structure Prepared by Chemical Precipitation. *Ceram. Int.* **2012**, 38, 5251–5255.
- (16) Hermet, P.; Fraysse, G.; Lignie, A.; Armand, P.; Papet, P. Density Functional Theory Predictions of the Nonlinear Optical Properties in  $\alpha$ -Quartz-Type Germanium Dioxide. *J. Phys. Chem. C* **2012**, *116*, 8692–8698.
- (17) Chae, S.; Mengle, K. A.; Lu, R.; Olvera, A.; Sanders, N.; Lee, J.; Poudeu, P. F. P.; Heron, J. T.; Kioupakis, E. Thermal Conductivity of Rutile Germanium Dioxide. *Appl. Phys. Lett.* **2020**, *117*, 102106.
- (18) Chae, S.; Mengle, K.; Bushick, K.; Lee, J.; Sanders, N.; Deng, Z.; Mi, Z.; Poudeu, P. F. P.; Paik, H.; Heron, J. T.; Kioupakis, E. Toward the Predictive Discovery of Ambipolarly Dopable Ultra-Wide-Band-Gap Semiconductors: The Case of Rutile GeO<sub>2</sub>. *Appl. Phys. Lett.* **2021**, *118*, 260501.
- (19) Chae, S.; Paik, H.; Vu, N. M.; Kioupakis, E.; Heron, J. T. Epitaxial Stabilization of Rutile Germanium Oxide Thin Film by Molecular Beam Epitaxy. *Appl. Phys. Lett.* **2020**, *117*, No. 072105.
- (20) Bushick, K.; Mengle, K. A.; Chae, S.; Kioupakis, E. Electron and Hole Mobility of Rutile GeO<sub>2</sub> from First Principles: An Ultrawide-Bandgap Semiconductor for Power Electronics. *Appl. Phys. Lett.* **2020**, *117*, 182104.
- (21) Baur, W. H.; Khan, A. A. Rutile-Type Compounds. IV. SiO<sub>2</sub>, GeO<sub>2</sub> and a Comparison with Other Rutile-Type Structures. *Acta. Crystallogr. B. Struct.* **1971**, 27, 2133–2139.
- (22) Ono, S.; Tsuchiya, T.; Hirose, K.; Ohishi, Y. High-Pressure Form of Pyrite-Type Germanium Dioxide. *Phys. Rev. B* **2003**, *68*, No. 014103.
- (23) Prakapenka, V. P.; Shen, G.; Dubrovinsky, L. S.; Rivers, M. L.; Sutton, S. R. High Pressure Induced Phase Transformation of SiO<sub>2</sub> and GeO<sub>2</sub>: Difference and Similarity. *J. Phys. Chem. Solids* **2004**, *65*, 1537–1545.
- (24) Filatova, E. O.; Sokolov, A. A.; Kozhevnikov, I. V.; Taracheva, E. Y.; Grunsky, O. S.; Schaefers, F.; Braun, W. Investigation of the Structure of Thin HfO<sub>2</sub> Films by Soft x-Ray Reflectometry Techniques. *J. Phys.: Condens. Matter* **2009**, *21*, No. 185012.
- (25) Makeswaran, N.; Das, D.; Zade, V.; Gaurav, P.; Shutthanandan, V.; Tan, S.; Ramana, C. V. Size- and Phase-Controlled Nanometer-Thick  $\beta$ -Ga<sub>2</sub>O<sub>3</sub> Films with Green Photoluminescence for Optoelectronic Applications. *ACS Appl. Nano Mater.* **2021**, *4*, 3331–3338.
- (26) Manandhar, S.; Battu, A. K.; Tan, S.; Panat, R.; Shutthanandan, V.; Ramana, C. V. Effect of Ti Doping on the Crystallography, Phase, Surface/Interface Structure and Optical Band Gap of Ga<sub>2</sub>O<sub>3</sub> Thin Films. *J. Mater. Sci.* **2019**, *54*, 11526–11537.
- (27) Ramana, C. V.; Ait-Salah, A.; Utsunomiya, S.; Becker, U.; Mauger, A.; Gendron, F.; Julien, C. M. Structural Characteristics of Lithium Nickel Phosphate Studied Using Analytical Electron Microscopy and Raman Spectroscopy. *Chem. Mater.* **2006**, *18*, 3788–3794.

- (28) Kumar, M.; Kumar, A.; Abhyankar, A. C. Influence of Texture Coefficient on Surface Morphology and Sensing Properties of W-Doped Nanocrystalline Tin Oxide Thin Films. *ACS Appl. Mater. Interfaces* **2015**, *7*, 3571–3580.
- (29) Own, C. S.; Sinkler, W.; Marks, L. D. Rapid Structure Determination of a Metal Oxide from Pseudo-Kinematical Electron Diffraction Data. *Ultramicroscopy* **2006**, *106*, 114–122.
- (30) Banerjee, D.; Mukherjee, S.; Chattopadhyay, K. K. Controlling the Surface Topology and Hence the Hydrophobicity of Amorphous Carbon Thin Films. *Carbon* **2010**, *48*, 1025–1031.
- (31) Ramana, C. V.; Smith, R. J.; Hussain, O. M.; Julien, C. M. On the Growth Mechanism of Pulsed-Laser Deposited Vanadium Oxide Thin Films. *Mater. Sci. Eng., B* **2004**, *111*, 218–225.
- (32) Schneider, C. A.; Rasband, W. S.; Eliceiri, K. W. NIH Image to ImageJ: 25 Years of Image Analysis. *Nat. Methods* **2012**, *9*, 671–675.
- (33) Murphy, N. R.; Grant, J. T.; Sun, L.; Jones, J. G.; Jakubiak, R.; Shutthanandan, V.; Ramana, C. V. Correlation between Optical Properties and Chemical Composition of Sputter-Deposited Germanium Oxide (GeO<sub>x</sub>) Films. *Opt. Mater.* **2014**, *36*, 1177–1182.
- (34) Pennington, A. M.; Okonmah, A. I.; Munoz, D. T.; Tsilomelekis, G.; Celik, F. E. Changes in Polymorph Composition in P25-TiO<sub>2</sub> during Pretreatment Analyzed by Differential Diffuse Reflectance Spectral Analysis. *J. Phys. Chem. C* **2018**, *122*, 5093–5104
- (35) Gutierrez, G.; Sundin, E. M.; Nalam, P. G.; Zade, V.; Romero, R.; Nair, A. N.; Sreenivasan, S.; Das, D.; Li, C.; Ramana, C. V. Interfacial Phase Modulation-Induced Structural Distortion, Band Gap Reduction, and Nonlinear Optical Activity in Tin-Incorporated Ga<sub>2</sub>O<sub>3</sub>. *J. Phys. Chem. C* **2021**, *125*, 20468–20481.
- (36) Rubio, E. J.; Ramana, C. V. Tungsten-Incorporation Induced Red-Shift in the Bandgap of Gallium Oxide Thin Films. *Appl. Phys. Lett.* **2013**, *102*, 191913.
- (37) Battu, A. K.; Manandhar, S.; Shutthanandan, V.; Ramana, C. V. Controlled Optical Properties via Chemical Composition Tuning in Molybdenum-Incorporated  $\beta$ -Ga<sub>2</sub>O<sub>3</sub> Nanocrystalline Films. *Chem. Phys. Lett.* **2017**, *684*, 363–367.
- (38) Rai, R. C. Analysis of the Urbach Tails in Absorption Spectra of Undoped ZnO Thin Films. *J. Appl. Phys.* **2013**, *113*, 153508.
- (39) Vargas, M.; Rubio, E. J.; Gutierrez, A.; Ramana, C. V. Spectroscopic Ellipsometry Determination of the Optical Constants of Titanium-Doped WO<sub>3</sub> Films Made by Co-Sputter Deposition. *J. Appl. Phys.* **2014**, *115*, 133511.
- (40) Wemple, S. H. Refractive-Index Behavior of Amorphous Semiconductors and Glasses. *Phys. Rev. B* **1973**, *7*, 3767–3777.
- (41) Pajasová, L. Optical Properties of GeO<sub>2</sub> in the Ultraviolet Region. *Czech. J. Phys.* **1969**, *19*, 1265–1270.